Advanced Fiber Materials
https://doi.org/10.1007/s42765-024-00420-w

RESEARCH ARTICLE

A Highly Sensitive Coaxial Nanofiber Mask for Respiratory Monitoring Assisted with Machine Learning

Boling Lan[1] · Cheng Zhong[1] · Shenglong Wang[1] · Yong Ao[1] · Yang Liu[1] · Yue Sun[1] · Tao Yang[1] · Guo Tian[1] · Longchao Huang[1] · Jieling Zhang[1] · Weili Deng[1] · Weiqing Yang[1,2]

Received: 21 January 2024 / Accepted: 8 April 2024
© Donghua University, Shanghai, China 2024

Abstract
Respiration is a critical physiological process of the body and plays an essential role in maintaining human health. Wearable piezoelectric nanofiber-based respiratory monitoring has attracted much attention due to its self-power, high linearity, non-invasiveness, and convenience. However, the limited sensitivity of conventional piezoelectric nanofibers makes it difficult to meet medical and daily respiratory monitoring requirements due to their low electromechanical conversion efficiency. Here, we present a universally applicable, highly sensitive piezoelectric nanofiber characterized by a coaxial composite structure of polyvinylidene fluoride (PVDF) and carbon nanotube (CNT), which is denoted as PS-CC. Based on elucidating the enhancement mechanism from the percolation effect, PS-CC exhibits excellent sensing performance with a high sensitivity of 3.7 V/N and a fast response time of 20 ms for electromechanical conversion. As a proof-of-concept, the nanofiber membrane is seamlessly integrated into a facial mask, facilitating accurate recognition of respiratory states. With the assistance of a one-dimensional convolutional neural network (CNN), a PS-CC-based smart mask can recognize respiratory tracts and multiple breathing patterns with a classification accuracy of up to 97.8%. Notably, this work provides an effective strategy for monitoring respiratory diseases and offers widespread utility for daily health monitoring and clinical applications.

Keywords PVDF/CNT · Coaxial nanofiber · High-sensitivity · Smart mask · Machine learning · Respiratory monitoring

1 Introduction

Respiration is an essential physiological behavior throughout the complete human life and encapsulates a great deal of physiological information about health and potential diseases in clinical medicine [1–6]. Gaining proactive insight and analyzing this physiological information can help to prevent malignant diseases [7–11]. For example, obstructive apnea syndrome (OAS) and lung dysfunction (LD) can be detected and prevented by respiratory statuses, such as abnormal breath volume and duration [12–18]. Consequently, effective and precise monitoring of daily physiological respiratory has emerged as necessary for disease prevention, exerting a profound impact on the overall health and safety of individuals.

At present, conventional medical monitoring equipment, such as sleep apnea monitoring equipment, modern imaging, and other treatments, can provide an effective diagnosis for OAS, LD, and other related diseases, but the bulky size, high price, and unsatisfactory convenience of these devices limit their use in broader medical situations, thus highlighting the need to overcome these significant limitations [19–21]. Personalized monitoring based on self-powered sensors is gradually emerging due to its unique advantages [22–28], transforming the traditional treatment-centered paradigm into one of personalized preventive-based health monitoring. Currently, wearable electronic devices for respiratory monitoring based on various principles, such as piezoelectric [29–31], piezoresistive [32–34], and triboelectric effect [35–37] have been widely developed. Notably, respiratory monitoring

✉ Weili Deng
weili1812@swjtu.edu.cn

✉ Weiqing Yang
wqyang@swjtu.edu.cn

[1] Key Laboratory of Advanced Technologies of Materials (Ministry of Education), School of Materials Science and Engineering, Southwest Jiaotong University, Chengdu, Sichuan 610031, People's Republic of China

[2] Research Institute of Frontier Science, Southwest Jiaotong University, Chengdu, Sichuan 610031, People's Republic of China

Published online: 14 May 2024

technologies based on piezoelectric nanofibers are preferred due to their compelling advantages, such as flexibility, good linearity, low cost, lightweight, and good breathability [16]. To obtain piezoelectric materials with superior performance for precise monitoring, numerous methodologies have been exhaustively investigated, among which the doping of either conductive or nonconductive nanoparticles has been proven to be effective in enhancing the electrical output of piezoelectric polymers [38–43]. For example, Yang et al. [44, 45] successfully achieved the enhancement of piezoelectric output by integrating MXene into polyvinylidene fluoride (PVDF), leveraging the interfacial polarization effect and nanolimited domain effect. Concurrently, Feng et al. [46] constructed a cavitation layer by introducing ZnO particles into electrospun PVDF nanofibers, and the d_{33} coefficient of the nanofibers was dramatically increased due to the profound impact of cavitation, which effectively improved the energy conversion efficiency of ultrasound. However, despite these novel and effective processes for enhancing the performance of traditional piezoelectric polymers, challenges persist, including the propensity for dopant agglomeration and the resulting inhomogeneity in sensing performance. These issues pose obstacles to achieving high-precision respiratory monitoring using piezoelectric polymers [47–49]. Therefore, forming a large-scale uniform piezoelectric polymer functional layer to realize highly sensitive sensing in wearable respiratory monitoring remains a major challenge.

Here, we innovatively prepared coaxial PVDF/carbon nanotube nanofibers with large-scale homogeneous dispersion of CNT nanoparticles by coaxial electrospinning to achieve high sensitivity and fast response time for respiratory monitoring. PVDF/CNT nanofiber membranes with adjustable CNT concentrations were prepared by coaxial electrospinning, and the effects of the CNT content on their output performance were systematically investigated. The piezoelectric sensors prepared from coaxial composite PVDF/CNT have a high sensitivity of up to 3.7 V/N and a fast response time of 20 ms, demonstrating excellent performance that is comparable to that of reported sensors. On this basis, a PS-CC-based smart mask was constructed for respiratory classification and respiratory tract monitoring, in which the recognition accuracy can reach up to 97.8% with the assistance of a one-dimensional convolutional neural network algorithm. This fabrication strategy is proposed to provide insight into future respiratory monitoring and intelligent devices.

2 Results and Discussion

2.1 Overall Schematic of Coaxial Nanofibers Applied to Respiratory Monitoring

Figure 1a schematically depicts the three main states of the respiratory tract, including the unobstructed state (US_1), the middle state (MS_2), and the obstructed state (OS_3) [50]. These different respiratory states have different respiratory rhythms and gas volumes, so different respiratory states require different durations to obtain sufficient oxygen (Fig. 1b). In US_1, due to the unobstructed structure, the volume of inhaled air reaches its maximum point in a short time. Conversely, both the gas volume of inhaled air and the duration of inspiration in OS_3 followed an opposite trend to that of US_1, while MS_2 was between US_1 and OS_3. With US_1 defined as the baseline for normal physiological respiration, the gas volume showed a decreasing trend in US_1, MS_2, and OS_3 at the same time. Similarly, under the equalizing gas volume among the three states, the duration of respiration gradually increased. These intricate dynamics are visually depicted in Fig. 1c. Due to the complexity of the signals, a high-accuracy on-mask piezoelectric sensor (PS-CC) with a coaxial composite structure is proposed for respiratory monitoring (Fig. 1d). The PS-CC is composed of a PVDF/CNT coaxial nanofiber membrane, Ag electrode, and protective layer polyurethane (PU) medical tape (Fig. S1, Supporting Information). To establish a mask respiratory monitoring platform, respiratory biomechanics were first validated based on finite element simulation. COMSOL simulation (Fig. S2, Supporting Information) was performed to determine the pressures exerted under normal, middle, and deep respiration conditions. The results show the nonuniform and position-dependent nature of the pressure distribution in the mask. Moreover, the vibration of the mask was measured in real-time by a laser vibrometer. When the mask does not vibrate, there is no electrical signal output; when the body breathes, it vibrates and generates the electrical signal (Fig. 1e, f and Movie S1, Supporting Information). The resulting vibration amplitude is mainly concentrated in the areas of the mouth and nose, which is consistent with the finite element simulation. Based on these results, the PS-CC was installed in the positions of the mask corresponding to the mouth and nose (Fig. S3, Supporting Information).

This deliberate positioning maximizes the pressure propagation derived from the respiratory process, thus collecting the respiratory signal of the human physiological state more accurately. Furthermore, the developed PS-CC-based smart mask combined with machine learning algorithms enables the acquisition of storage and display of monitoring results at a computer terminal, forming

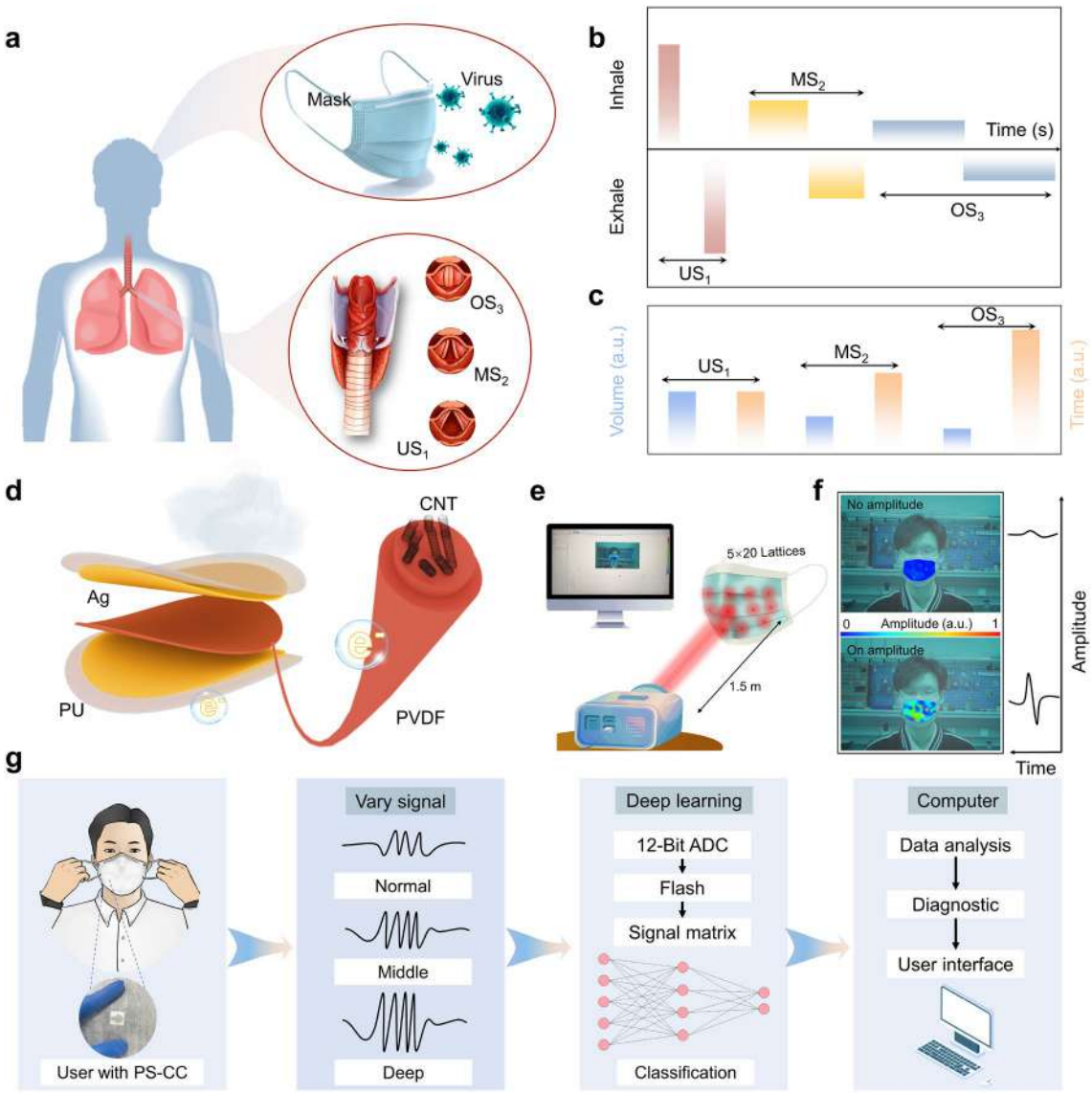

Fig. 1 Overall concept of respiratory monitoring. **a** Schematic illustration of the respiratory system of the human body, including three different respiratory tracts, US_1, MS_2, and OS_3. **b** Schematic illustration of the inhalation and exhalation states of US_1, MS_2, and OS_3 during a cycle. **c** Comparison of volume and time between US_1, MS_2, and OS_3. **d** Schematic showing the structure of the PS-CC. **e** Schematic of laser vibration measurement for the mask. The test distance was 1.5 m and the mask had a lattice profile of 5×20. **f** Voltage schematic illustration of the real-time detection of mask vibrations. **g** Schematic illustration of the machine learning-assisted adaptive respiratory monitoring

an adaptive respiratory monitoring system, as shown in Fig. 1g. This innovation is positioned to establish a framework for the eventual realization of an integrated, intelligent, and user-friendly respiratory monitoring paradigm.

2.2 Structural and Component Characterization of the Coaxial Nanofibers

To demonstrate the construction of the developed PVDF/CNT coaxial nanofiber fabricated through modified coaxial electrospinning (Fig. S4, Supporting Information), the surface morphology and size of the PVDF/CNT coaxial nanofibers were analyzed. Figure 2a shows that the produced PVDF/CNT coaxial nanofibers have a straight configuration without any nodular formations and the majority of the nanofibers range in diameter from 0.1 to 0.3 μm (Fig. S5, Supporting Information), indicating good homogeneity. The doped CNTs are short multiwalled carbon nanotubes with 20–30 nm outer diameters, as shown in Fig. 2b. Furthermore, the TEM image captures the coaxial structure of the PVDF shell and the CNT core (Fig. 2c). To intuitively analyze the phase structure composition of the

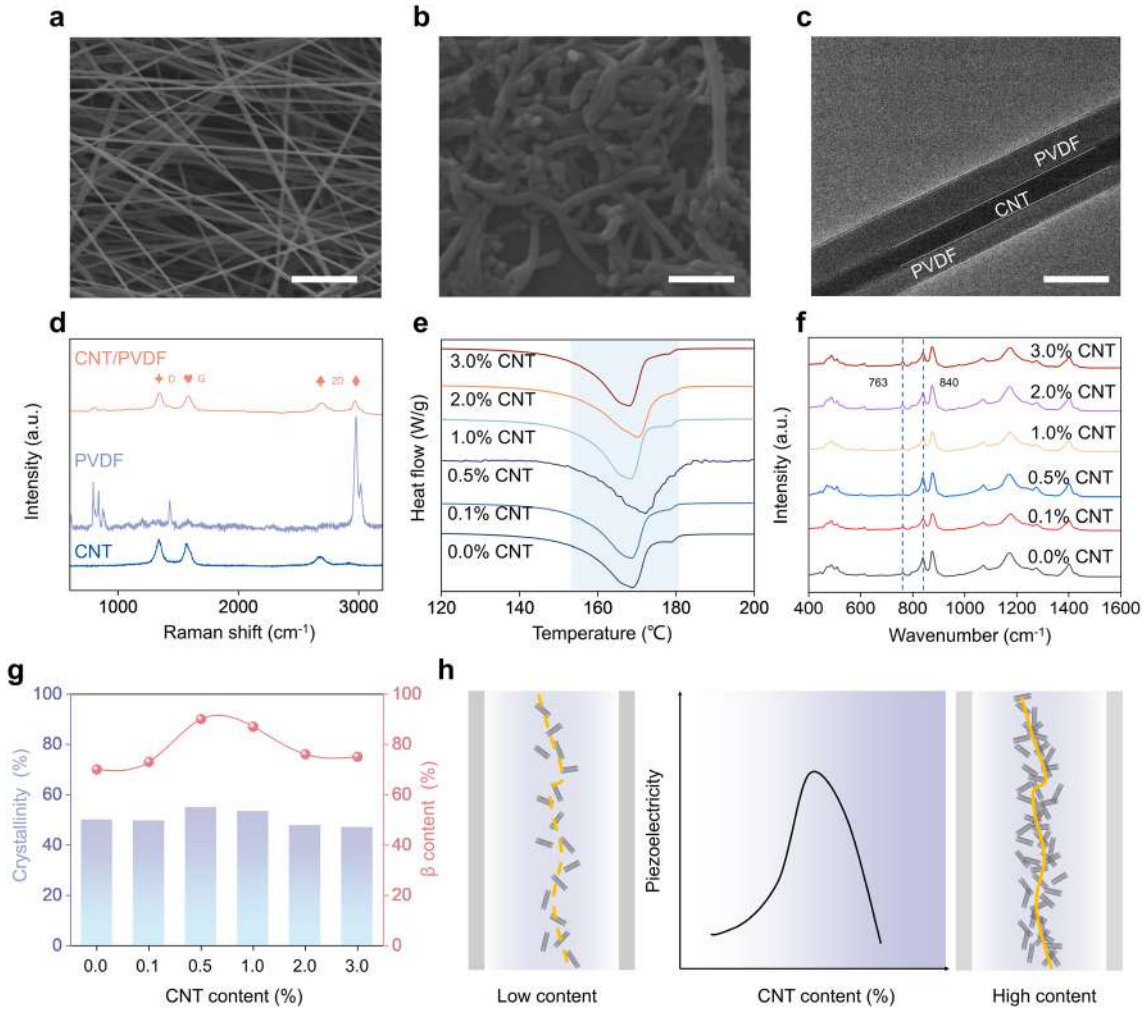

Fig. 2 Material characterization and mechanism analysis. **a** SEM image of the PVDF/CNT nanofiber. Scale bar: 3 μm. **b** SEM image of CNT. Scale bar: 1 μm. **c** TEM image of the PVDF/CNT nanofiber. Scale bar: 200 nm. **d** Raman spectra of the PVDF/CNT nanofiber membrane, pristine PVDF, and CNT. **e** DSC of PVDF/CNT nanofiber membranes with different CNT contents. **f** FTIR of PVDF/CNT nanofiber membranes with different CNT contents. **g** Crystallinity of the matrix and the proportion of the β-phase in the above samples vary with the CNT content. **h** Schematic of composites near the percolation effect

coaxial nanofibers, Raman spectroscopy was performed on the PVDF/CNT coaxial nanofibers, PVDF nanofibers, and pure CNTs, as shown in Fig. 2d. From the Raman spectra, three characteristic peaks of CNT emerge at 1340 cm^{-1} (D peak), 1576 cm^{-1} (G peak), and 2689 cm^{-1} (2D peak), and the main characteristic peaks of PVDF are at 794, 1430, and 2977 cm^{-1}, aligning with the established CNT and PVDF peaks, respectively. Moreover, all the peaks of the developed PVDF/CNT have the major characteristic peaks of the PVDF nanofiber and pure CNT, proving the successful construction of the PVDF/CNT coaxial nanofibers. In principle, the content of the conductive filler intuitively affects the performance of PVDF [43]. To determine the optimal CNT content and decouple the influence of CNT on the piezoelectric phase of PVDF, it is necessary to quantitatively calculate the crystallinity and β-phase content of PVDF with different CNT contents. To this end, differential scanning calorimetry (DSC) (Fig. 2e) and Fourier transform infrared (FTIR) spectroscopy (Fig. 2f) were performed. The degree of crystallinity can be calculated by Eq. (1) [44]:

$$\sigma_c = \frac{\Delta H_m}{(1-\varphi)\Delta H_0} \times 100\% \quad (1)$$

where σ_c is the degree of crystallinity in the sample, ΔH_0 is the melting enthalpy of the test sample, φ is the weight fraction of CNT and ΔH_m is the standard melting enthalpy of the pure PVDF crystal with a value of 103.4 J g^{-1}. Furthermore, the β-phase content in the sample can be obtained by Eq. (2) [39, 40]:

$$F(\beta) = \frac{A_\beta}{1.26A_\alpha + A_\beta} \quad (2)$$

where $F(\beta)$ is the content of the β-phase. A_β and A_α are the intensities of the characteristic peaks of the β-phase at 840 cm^{-1} and the α-phase at 763 cm^{-1}, respectively.

The results presented in Fig. 2g show that both the crystallinity and β-phase content gradually increase with increasing CNT content up to 0.5%. When this content exceeds 0.5%, both characteristics show a gradual decreasing trend. To illustrate this phenomenon, the percolation effect is introduced into the system [44]. With the gradual increase in the CNT concentration, more interfaces are formed inside the PVDF membrane, which is conducive to the enhancement of piezoelectricity. When the content exceeds a certain threshold, the aggregation of conductive particles forms conductive pathways inside the nanofibers, which reduces the piezoelectric output. A corresponding schematic and simulation diagrams are shown in Fig. 2h and Fig. S6 (Supporting Information). Therefore, CNT coaxial nanofibers with 0.5% CNT were chosen as the experimental condition to obtain the optimal performance.

2.3 Piezoelectric Properties of Coaxial Nanofibers

To further verify the electrical output performance and meet the daily needs of respiratory monitoring, we tested the electromechanical performance of the PS-CC_x based on servo motors (x represents the amount of CNT with values of 0, 0.1, 0.5, 1.0, 2.0, and 3.0%, as shown in Fig. 3a). Under a constant pressure of 0.5 N, the voltage outputs of PS-CC_0, PS-$CC_{0.1}$, PS-$CC_{0.5}$, PS-$CC_{1.0}$, PS-$CC_{2.0}$, and PS-$CC_{3.0}$ clearly increase and then decrease. When the CNT content exceeds 0.5%, it exhibits the highest voltage output of 1.8 V

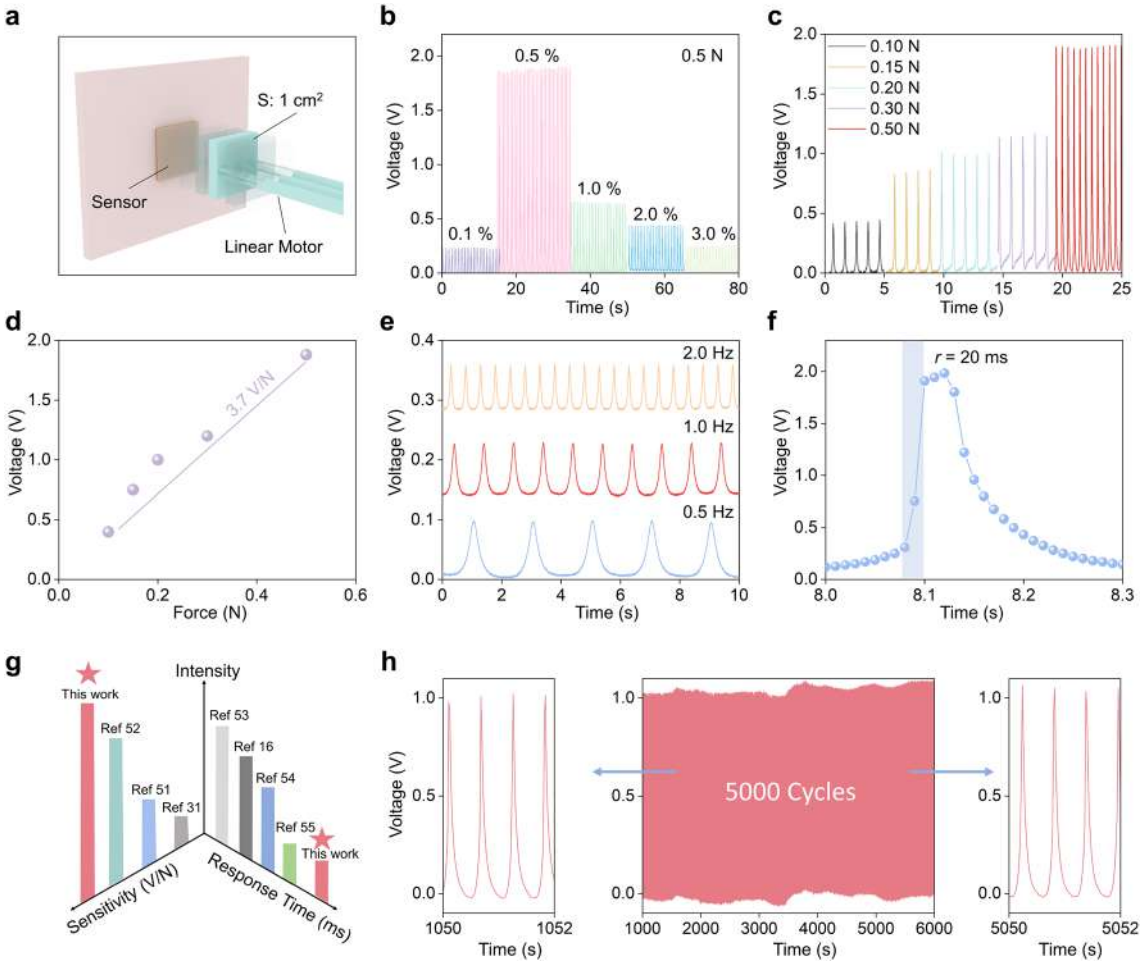

Fig. 3 Electrical performance of the designed PS-$CC_{0.5}$. **a** Schematic diagram showing the measurement of the PS-CC under the pressing model. **b** Voltage output of PS-CC with different CNT contents under the same pressure. **c** Voltage output of PS-$CC_{0.5}$ with different forces ranging from 0.1 to 0.5 N. **d** Sensitivity of PS-$CC_{0.5}$. **e** The voltage response of PS-$CC_{0.5}$ under the same force at various frequencies. **f** Response time of PS-$CC_{0.5}$. **g** Characteristic comparisons of the sensitivity and response time between this work and the recorded respiratory sensor. **h** Durability test of the sensor after more than 5000 cycles with no signs of fatigue

(Fig. 3b). This trend is consistent with the previous mechanism analysis (Fig. 2h), further proving that PS-$CC_{0.5}$ has the best performance in the experimental view. Therefore, the PS-$CC_{0.5}$-design serves as the foundation for subsequent experiments. In respiratory monitoring, an accurate and rapid response is essential for those key physiological signals, including respiratory sensitivity (RS), respiratory frequency (RF), and response time (RT). To further investigate the RS of PS-$CC_{0.5}$, different forces were applied to PS-$CC_{0.5}$, and the corresponding results are presented in Fig. 3c. With increasing force from 0.1 to 0.5 N, the voltage output increased from 0.45 to 1.95 V. It is proposed that the dipole deflection of the nanofibers increases with increasing force, resulting in a higher voltage output. The RS of the PS-CC is defined by Eq. (3):

$$RS = \frac{\Delta V}{\Delta F} \tag{3}$$

where ΔV is the voltage difference and ΔF is the force difference. Based on Formula (3), the RS was calculated to be 3.7 V/N (Fig. 3d), indicating favorable sensitivity.

Figure 3e, f presents the RF and RT of PS-$CC_{0.5}$ at different frequencies (0.5, 1, and 2 Hz) under the same pressure conditions. The results show that PS-$CC_{0.5}$ responds accurately to stimuli of different frequencies and has a rapid response (20 ms), demonstrating its favorable performance. By comparing RS [31, 51, 52], and RT [16, 53–55] with other developed respiratory sensors, the PS-$CC_{0.5}$-proposed in this work has clear advantages (Fig. 3g). Furthermore, it maintains excellent electrical stability even after 5000 cycles (Fig. 3h), indicating the long service life and high stability of PS-$CC_{0.5}$. Therefore, PS-$CC_{0.5}$ is characterized by its high sensitivity, short RT, and robustness, making it suitable for precise and long-term respiratory monitoring.

2.4 Demonstration of Coaxial Nanofibers for Respiratory Monitoring Applications

Based on the excellent sensing performance, an intelligent respiratory monitoring platform with a PS-$CC_{0.5}$-based smart mask (PSM) was developed and the characteristics of respiratory gas volume were analyzed to classify respiratory status (US_1, MS_2, and OS_3). The detection schematic and physical diagram of the PSM (as worn by the tester) are shown in Fig. 4a and Fig. S7. When the body engages in the respiratory cycle, inhalation gas is transmitted to the PSM and expands inward, which generates corresponding electrical signals (Fig. 4b). Conversely, the PSM expands outward and produces opposing signals (Fig. 4c). The processes and results are shown in Fig. 4d. The integral of this curve over time can represent the respiratory air volume to some extent, such as pink for the inhaled air volume and purple for the exhaled air volume. Different respiratory patterns have corresponding air volumes, so US_1, MS_2, and OS_3 are respectively correlated with slow, normal, and deep breathing. The inhalation and exhalation processes of human body were simultaneously measured by PSM and a commercial electronic spirometer (Fig. S8, Supporting Information). Figure 4e shows the relationship between the time and voltage of inhalation tested by the PSM under three respiratory states: slow, normal, and deep. The statistical results show that the respiratory pattern changes from slow to normal and to deep, and the air volume gradually increases (Fig. 4f). Moreover, the FVC (the maximum volume of air that can be exhaled as soon as possible after inhalation) curves of the volume of exhaled air over time were measured by a commercial electronic spirometer [56]. From the statistical results in Fig. 4g–h, the air volume trends for different states are in good agreement with the actual situation. This favorable performance is attributed to the high RS of the PSM for respiratory monitoring. In addition, a wide variety of respiratory states are characterized in daily life. To adapt these states in daily application, the PSM was extended to monitor various respiratory states, such as fast, no breathing, and coughing (Fig. 4i, Fig. S9–10, Movie S2, Supporting Information). The results show that there are significant discrepancies in respiratory intensity and rate in multiple respiratory styles, such as the deep style producing higher voltage than that of the normal style (Fig. 4j). Additionally, the respiratory rate can be inferred from the number of peaks. The rate is 30 breaths/min for the normal style and up to 120 breaths/min for the fast style. These data, derived from PSM, can provide convenient and quick respiratory references in medicine to a certain extent. Due to the excellent performance of PSMs, they can be further used as recognition elements in human−machine interfaces to provide more efficient and accurate respiratory monitoring. Many methods are used in the sequence modeling of signals, such as recurrent neural networks and long- and short-term memory. In particular, the one-dimensional convolutional neural network (CNN) algorithm with multiple processing layers is a simple and feasible method, and each layer can learn and express more abstract and higher-level input data. The user wears the PSM to monitor six different breathing states, and the output signals in each state are randomly divided into training, validation, and testing sets at a ratio of 8:1:1. Figure 4k and Fig. S11 show the variation process of training, testing accuracy and training loss for the datasets, indicating that the proposed model can achieve high classification accuracy and robustness. The confusion matrix between the predicted labels and real labels in the test set is shown in Fig. 4l. After 200 training sessions, the system could recognize different breathing states with an average prediction accuracy of 97.8%. Based on the excellent

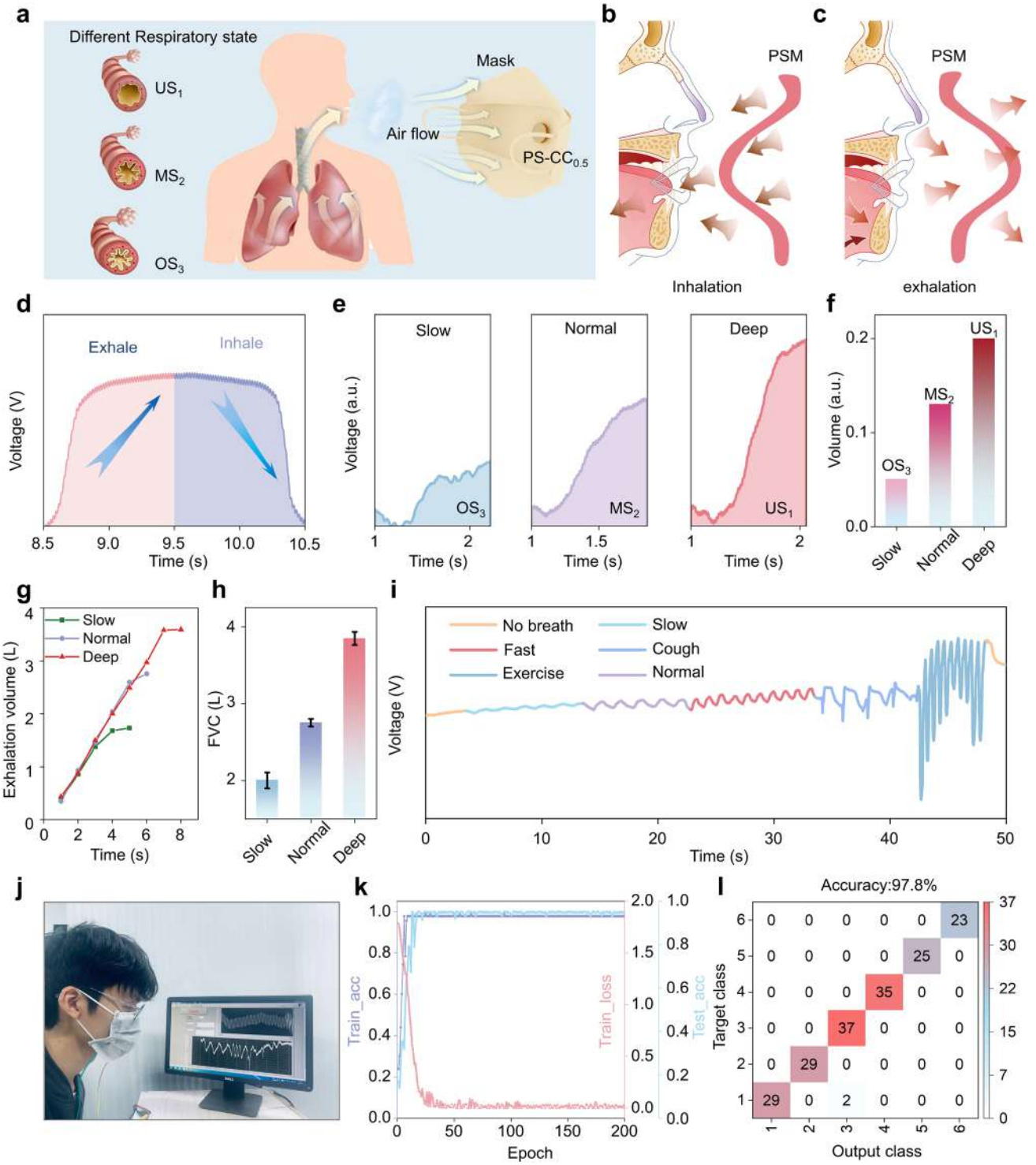

Fig. 4 Demonstration of the PSM adaptive respiratory monitoring system. **a** Schematic diagram of the mask with a PSM for respiratory monitoring. Schematic diagram of PSM changes during inhalation (**b**) and exhalation (**c**). **d** An electrical signal corresponds to a complete respiratory cycle. **e** Voltage signals of slow (OS_3), normal (MS_2), and deep (US_1) styles are recorded by the PSM. **f** Integral plot of air volume for inhalation in three respiratory states. **g** The time-domain volume of commercial sensors recorded the inspiratory air volume in three respiratory states. **h** The maximum inspiratory air volume. **i** Measurement result of different respiratory styles under the PSM. **j** Photo of respiratory monitoring with PSM. **k** Evaluation of the classification accuracy, training accuracy, and loss function over 200 epochs. **l** Confusion matrix for respiratory recognition. The target class refers to the collected signal types and the output class refers to the results recognized with the assistance of machine learning

electromechanical conversion performance of PSMs, the developed PSM has significant potential in future smart medicine, human health, and respiratory monitoring.

3 Conclusion

In conclusion, we present a smart mask that incorporates a highly sensitive coaxial piezoelectric nanofiber membrane based on PVDF/CNT for respiratory monitoring. The nanofiber composite was fabricated by a coaxial electrospinning process that formed a uniform dispersion of CNT conductive particles. Due to the percolation effect, the performance of PSM is optimized at a CNT concentration of 0.5%, resulting in a high sensitivity of 3.7 V/N and a fast response time of 20 ms. Moreover, respiratory monitoring reaches a remarkably high accuracy of up to 97.8% for respiratory classification and successfully realizes respiratory monitoring due to the synergistic integration of the PSM and a CNN algorithm. This research provides a basis for future respiratory monitoring and shows promising prospects in the fields of artificial intelligence medical treatment and wearable electronics.

4 Experimental Section

4.1 Preparation of Solutions and Materials

First, 1.84 g of PVDF (MW ~ 180,000 g/mol, Sigma Aldrich) was dissolved in 5 mL of a mixed solution consisting of 3.25 mL of N–N-dimethylacetamide (Sigma Aldrich) and 1.75 mL of acetone (Sigma Aldrich). The mixture was heated and stirred in a water bath at 60 °C for 2 h to form a uniform mixture without bubbles as the shell structure. Then, another mixture was prepared by adding different amounts of CNT (short multiwalled, 20–30 nm outer diameter, 0.5–2 μm length, ≥ 98%, Aladdin), followed by sonication for 30 min and stirring for 60 min to form the core layer.

4.2 Electrospinning Process and Fabrication of the Sensor

The electrospinning process requires a high-voltage source, a syringe pump, and a drum collector. Coaxial electrospinning was performed using a 22/17-gauge blunt-end coaxial stainless steel needle. The feed rates of the inner and outer layer solutions were 0.5 and 0.4 mL/h, respectively. The needle was connected to a high-voltage supply at 14 ± 1 kV, and the PVDF/CNT nanofibers were collected using a drum collector covered with aluminum foil at 1000 r/min. The receiving plate was kept at a distance of 10.5 ± 1 cm from the needle, and the electrospinning time was 2 h. During nanofiber electrospinning, the ambient material was air at a temperature of 25 °C and 50% humidity. Then, the membrane was put into an oven for 12 h at 60 °C. Then, silver was magnetron sputtered onto the surface of an annealed PVDF/CNT piezoelectric membrane for 15 min and used as an electrode, and the electrode was removed with a copper wire and sealed on both sides with PU tape in the same way as in previous work [39, 40].

4.3 Finite Element Analysis and Laser Vibration Detection

Finite element analysis was employed to analyze the vibration modes of the designed membrane and the breakdown of the conductive filler in PVDF. First, due to the complexity of the mask network at the microscopic scale, we simplified it into a membrane with a Young's modulus of 840 M and a Poisson's ratio of 0.4. Then, for the breakdown simulation, we used PVDF as the basis and CNT particles as the conductive filler particles. To show the breakdown characteristics more intuitively, we set the thermal conductivity of PVDF to 0.25 W/(m·K), the electrical conductivity of CNT to 5.998×10^7 S/m, and the relative permittivity to 1. When the relative conductive particle content changes, we simulate the change rule of the breakdown characteristics. The laser vibrometer model used was an LV-SC400, and a quick signal analyzer was used for analysis and modeling. First, the face of the mask was processed for positioning, the mesh was dissected, and its value was set to 5×60. The maximal setting of velocity in the control box of VD19 DD29 was 10 mm s^{-1} v^{-1}, the maximal setting of displacement was 20 mm/V, and the sample rate and the number of fast Fourier transform points were set to 500 in the testing process.

4.4 Materials Characteristics and Measurement of Electric Performance

The coaxial PVDF/CNT piezoelectric nanofiber and CNT morphologies were studied by field emission scanning electron microscopy (FESEM, JSM-7800f). The crystal content and phase structure of the PVDF, CNT, and composites were determined by Raman spectroscopy (HORIBA JobinYvon XploRA ONE, 532 nm laser), differential scanning calorimetry (DSC; TGA/DSC 3+, Mettler Toledo), and FTIR (Nicolet 5700 Spectrometer). Then, the voltage output of the PSM was recorded by a Keithley-6514 system electrometer, and the signal was collected and analyzed by a data acquisition card.

4.5 Deep Learning for Voice Pattern Recognition

A three-layer 1D-CNN was constructed for data feature extraction and automatic recognition of input-collected

respiratory signals. PSM was used to continuously collect six respirator signals as the target class dataset, and each signal was recorded 20 times, with a length of each dataset of 1000; then, the data were enhanced four times. The samples of each object were randomly divided into a training set, a validation set, and a test set at a ratio of 8:1:1. We first trained the model with 80% of the data, then calibrated the model with 10% of the data, and finally used the remaining 10% of the data to further test the corrected optimal model parameters. During each training epoch, the classification accuracy, learning rate, and loss function were evaluated to test the deep learning results. With the assistance of the 1D-CNN algorithm, 200 training periods could achieve respiratory recognition, and then the classification and analysis were carried out in terms of classification accuracy, rate, and loss function.

Supplementary Information The online version contains supplementary material available at https://doi.org/10.1007/s42765-024-00420-w.

Acknowledgements This research was financially supported by the Sichuan Science and Technology Program (No. 2023NSFSC0313) and the Basic Research Cultivation Project of Southwest Jiaotong University (No. 2682023KJ024). We are thankful for the help from the Analysis and Testing Center of Southwest Jiaotong University.

Data availability The data underlying this study are available in the published article. The raw data can be obtained by email contact when readers need it.

Declarations

Conflict of interest The authors state that there are no conflicts of interest to disclose.

References

1. Hu H, Huang H, Li M, Gao X, Yin L, Qi R, Wu RS, Chen X, Ma Y, Shi K, Li C, Maus TM, Huang B, Lu C, Lin M, Zhou S, Lou Z, Gu Y, Chen Y, Lei Y, Wang X, Wang R, Yue W, Yang X, Bian Y, Mu J, Park G, Xiang S, Cai S, Corey PW, Wang J, Xu S. A wearable cardiac ultrasound imager. *Nature*. **2023**;*613*:667.
2. Qian X, Chen X, Zhu L, Zhang QM. Fluoropolymer ferroelectrics: Multifunctional platform for polar-structured energy conversion. *Science*. **2023**;*380*:eadg0902.
3. Deng W, Zhou Y, Libanori A, Chen G, Yang W, Chen J. Piezoelectric nanogenerators for personalized healthcare. *Chem Soc Rev*. **2022**;*51*:3317.
4. Chen G, Li Y, Bick M, Chen J. Smart textiles for electricity generation. *Chem Rev*. **2020**;*120*:3668.
5. Yu X, Xie Z, Yu Y, Lee J, Vazquez-Guardado A, Luan H, Ruban J, Ning X, Akhtar A, Li D, Ji B, Liu Y, Sun R, Cao J, Huo Q, Zhong Y, Lee C, Kim S, Gutruf P, Zhang C, Xue Y, Guo Q, Chempakasseril A, Tian P, Lu W, Jeong J, Yu Y, Cornman J, Tan C, Kim B, Lee K, Feng X, Huang Y, Rogers J. Skin-integrated wireless haptic interfaces for virtual and augmented reality. *Nature*. **2019**;*575*:473.
6. Song Y, Tay R, Li J, Xu C, Min J, Sani E, Kim G, Heng W, Kim I, Gao W. 3D-printed epi fluidic electronic skin for machine learning–powered multimodal health surveillance. *Sci Adv*. **2023**;*9*:eadi6492.
7. Xu Y, De la Paz E, Paul A, Mahato K, Sempionatto J, Tostado N, Lee M, Hota G, Lin M, Uppal A, Chen W, Dua S, Yin L, Wuerstle B, Deiss S, Mercier P, Xu S, Wang J, Cauwenberghs G. In-ear integrated sensor array for the continuous monitoring of brain activity and of lactate in sweat. *Nat Biomed Eng*. **2023**;*7*:1307.
8. Vinikoor T, Dzidotor G, Le T, Liu Y, Kan H, Barui S, Chorsi M, Curry E, Reinhardt E, Wang H, Singh P, Merriman M, D'Orio E, Park J, Xiao S, Chapman J, Lin F, Truong C, Prasadh S, Chuba L, Killoh S, Lee S, Wu Q, Chidambaram R, Lo K, Laurencin C, Nguyen T. Injectable and biodegradable piezoelectric hydrogel for osteoarthritis treatment. *Nat Commun*. **2023**;*14*:6257.
9. Wang M, Zhang J, Tang Y, Li J, Zhang B, Liang E, Mao Y, Wang X. Air-flow-driven triboelectric nanogenerators for self-powered real-time respiratory monitoring. *ACS Nano*. **2018**;*12*:6156.
10. Ye Z, Ling Y, Yang M, Xu Y, Zhu L, Yan Z, Chen P. A breathable, reusable, and zero-power smart face mask for wireless cough and mask-wearing monitoring. *ACS Nano*. **2022**;*16*:5874.
11. Shin J, Jeong S, Kim J, Choi Y, Choi J, Lee J, Kim S, Kim M, Rho Y, Hong S, Choi J, Grigoropoulos C, Ko S. Dynamic pore modulation of stretchable electrospun nanofiber filter for adaptive machine learned respiratory protection. *ACS Nano*. **2021**;*15*:15730.
12. Peng Z, Shi J, Xiao X, Hong Y, Li X, Zhang W, Cheng Y, Wang Z, Li W, Chen J, Leung MK, Yang Z. Self-charging electrostatic face masks leveraging triboelectrification for prolonged air filtration. *Nat Commun*. **2022**;*13*:7835.
13. Su Y, Chen G, Chen C, Gong Q, Xie G, Yao M, Tai H, Jiang Y, Chen J. Self-powered respiration monitoring enabled by a triboelectric nanogenerator. *Adv Mater*. **2021**;*33*: e2101262.
14. Zhong J, Li Z, Takakuwa M, Inoue D, Hashizume D, Jiang Z, Shi Y, Ou L, Nayeem M, Umezu S, Fukuda K, Someya T. Smart face mask based on an ultrathin pressure sensor for wireless monitoring of breath conditions. *Adv Mater*. **2022**;*34*: e2107758.
15. Khan Y, Ostfeld A, Lochner C, Pierre A, Arias A. Monitoring of vital signs with flexible and wearable medical devices. *Adv Mater*. **2016**;*28*:4373.
16. Fang Y, Xu J, Xiao X, Zou Y, Zhao X, Zhou Y, Chen J. A deep-learning-assisted on-mask sensor network for adaptive respiratory monitoring. *Adv Mater*. **2022**;*34*: e2200252.
17. Chen S, Qian G, Ghanem B, Wang Y, Shu Z, Zhao X, Yang L, Liao X, Zheng Y. Quantitative and real-time evaluation of human respiration signals with a shape-conformal wireless sensing system. *Adv Sci*. **2022**;*9*:2203460.
18. Ye L, Wu F, Xu R, Di Z, Lu J, Wang C, Dong A, Xu S, Xue L, Fan Z, Xu L, Li K, Li D, Kursumovic A, Zhao R, Tang R, Qiu L, Wang H, MacManus-Driscoll J, Jing Q, Li W, Yang H. Face mask integrated with flexible and wearable manganite oxide respiration sensor. *Nano Energy*. **2023**;*112*: 108460.
19. Corral-Penafiel J, Pepin J, Barbe F. Ambulatory monitoring in the diagnosis and management of obstructive sleep apnoea syndrome. *Eur Respir Rev*. **2013**;*22*:312.
20. Haick H, Broza Y, Mochalski P, Ruzsanyi V, Amann A. Assessment, origin, and implementation of breath volatile cancer markers. *Chem Soc Rev*. **2014**;*43*:1423.
21. Raichle M. Images of the mind: studies with modern imaging techniques. *Annu Rev Psychol*. **1994**;*45*:333.
22. Luo Y, Abidian MR, Ahn J-H, Akinwande D, Andrews AM, Antonietti M, Bao Z, Berggren M, Berkey CA, Bettinger CJ, Chen J, Chen P, Cheng W, Cheng X, Choi S-J, Chortos A, Dagdeviren C, Dauskardt RH, Di C-A, Dickey MD, Duan X, Facchetti A, Fan Z, Fang Y, Feng J, Feng X, Gao H, Gao W, Gong X, Guo CF, Guo X, Hartel MC, He Z, Ho JS, Hu Y, Huang Q, Huang Y, Huo F, Hussain MM, Javey A, Jeong U, Jiang C, Jiang X, Kang J, Karnaushenko D, Khademhosseini A, Kim D-H, Kim I-D, Kireev

D, Kong L, Lee C, Lee N-E, Lee PS, Lee T-W, Li F, Li J, Liang C, Lim CT, Lin Y, Lipomi DJ, Liu J, Liu K, Liu N, Liu R, Liu Y, Liu Y, Liu Z, Liu Z, Loh XJ, Lu N, Lv Z, Magdassi S, Malliaras GG, Matsuhisa N, Nathan A, Niu S, Pan J, Pang C, Pei Q, Peng H, Qi D, Ren H, Rogers JA, Rowe A, Schmidt OG, Sekitani T, Seo D-G, Shen G, Sheng X, Shi Q, Someya T, Song Y, Stavrinidou E, Su M, Sun X, Takei K, Tao X-M, Tee BCK, Thean AV-Y, Trung TQ, Wan C, Wang H, Wang J, Wang M, Wang S, Wang T, Wang ZL, Weiss PS, Wen H, Xu S, Xu T, Yan H, Yan X, Yang H, Yang L, Yang S, Yin L, Yu C, Yu G, Yu J, Yu S-H, Yu X, Zamburg E, Zhang H, Zhang X, Zhang X, Zhang X, Zhang Y, Zhang Y, Zhao S, Zhao X, Zheng Y, Zheng Y-Q, Zheng Z, Zhou T, Zhu B, Zhu M, Zhu R, Zhu Y, Zhu Y, Zou G, Chen X. Technology roadmap for flexible sensors. *ACS Nano*. **2023**;*17*:5211.

23. Yoon H, Choi J, Kim J, Kim J, Min J, Kim D, Jeong S, Lee JG, Bang J, Choi SH, Jeong Y, Kim CY, Ko SH. Adaptive epidermal bioelectronics by highly breathable and stretchable metal nanowire bioelectrodes on electrospun nanofiber membrane. *Adv Funct Mater*. **2024**. https://doi.org/10.1002/adfm.202313504.
24. Wang Z, Shi N, Zhang Y, Zheng N, Li H, Jiao Y, Cheng J, Wang Y, Zhang X, Chen Y, Chen Y, Wang H, Xie T, Wang Y, Ma Y, Gao X, Feng X. Conformal in-ear bioelectronics for visual and auditory brain-computer interfaces. *Nat Commun*. **2023**;*14*:4213.
25. Min S, Kim D, Joe D, Kim B, Jung Y, Lee J, Lee B, Doh I, An J, Youn Y, Joung B, Yoo C, Ahn H, Lee K. Clinical validation of a wearable piezoelectric blood-pressure sensor for continuous health monitoring. *Adv Mater*. **2023**;*35*: e2301627.
26. Li J, Carlos C, Zhou H, Sui J, Wang Y, Silva-Pedraza Z, Yang F, Dong Y, Zhang Z, Hacker TA, Liu B, Mao Y, Wang X. Stretchable piezoelectric biocrystal thin films. *Nat Commun*. **2023**;*14*:6562.
27. Feng T, Ling D, Li C, Zheng W, Zhang S, Li C, Emel'yanov A, Pozdnyakov AS, Lu L, Mao Y. Stretchable on-skin touchless screen sensor enabled by ionic hydrogel. *Nano Res*. **2024**;*17*:4462.
28. Park H, Park W, Lee CH. Electrochemically active materials and wearable biosensors for the in situ analysis of body fluids for human healthcare. *NPG Asia Mater*. **2021**;*13*:22.
29. Chen X, Li X, Shao J, An N, Tian H, Wang C, Han T, Wang L, Lu B. High-performance piezoelectric nanogenerators with imprinted P(VDF-TrFE)/$BaTiO_3$ nanocomposite micropillars for self-powered flexible sensors. *Small*. **2017**;*13*:1604245.
30. Panahi A, Hassanzadeh A, Moulavi A. Design of a low cost, double triangle, piezoelectric sensor for respiratory monitoring applications. *Sens Bio-Sens Res*. **2020**;*30*: 100378.
31. Le TT, Curry EJ, Vinikoor T, Das R, Liu Y, Sheets D, Tran KTM, Hawxhurst CJ, Stevens JF, Hancock JN, Bilal OR, Shor LM, Nguyen TD. Piezoelectric nanofiber membrane for reusable, stable, and highly functional face mask filter with long-term biodegradability. *Adv Funct Mater*. **2022**;*32*:2113040.
32. Moshizi S, Abedi A, Sanaeepur M, Pastras C, Han Z, Wu S, Asadnia M. Polymeric piezoresistive airflow sensor to monitor respiratory patterns. *J R Soc Interface*. **2021**;*18*:34875876.
33. Tian G, Shi Y, Deng J, Yu W, Yang L, Lu Y, Zhao Y, Jin X, Ke Q, Huang C. Low-cost, scalable fabrication of all-fabric piezoresistive sensors via binder-free, in-situ welding of carbon nanotubes on bicomponent nonwovens. *Adv Fiber Mater*. **2024**;*6*:120.
34. Yang T, Deng W, Chu X, Wang X, Hu Y, Fan X, Song J, Gao Y, Zhang B, Tian G, Xiong D, Zhong S, Tang L, Hu Y, Yang W. Hierarchically microstructure-bioinspired flexible piezoresistive bioelectronics. *ACS Nano*. **2021**;*15*:11555.
35. Yan Z, Wang L, Xia Y, Qiu R, Liu W, Wu M, Zhu Y, Zhu S, Jia C, Zhu M, Cao R, Li Z, Wang X. Flexible high-resolution triboelectric sensor array based on patterned laser-induced graphene for self-powered real-time tactile sensing. *Adv Funct Mater*. **2021**;*31*:2100709.
36. Zhao Z, Yan C, Liu Z, Fu X, Peng LM, Hu Y, Zheng Z. Machine-washable textile triboelectric nanogenerators for effective human respiratory monitoring through loom weaving of metallic yarns. *Adv Mater*. **2016**;*28*:10267.
37. Xi B, Wang L, Yang B, Xia Y, Chen D, Wang X. Boosting output performance of triboelectric nanogenerator based on $BaTiO_3$: La embedded nanofiber membrane for energy harvesting and wireless power transmission. *Nano Energy*. **2023**;*110*: 108385.
38. Liu J, Tian G, Yang W, Deng W. Recent progress in flexible piezoelectric devices toward human-machine interactions. *Soft Sci*. **2022**;*2*:22.
39. Lan B, Xiao X, Carlo AD, Deng W, Yang T, Jin L, Tian G, Ao Y, Yang W, Chen J. Topological nanofibers enhanced piezoelectric membranes for soft bioelectronics. *Adv Funct Mater*. **2022**;*32*:2207393.
40. Lan B, Yang T, Tian G, Ao Y, Jin L, Xiong D, Wang S, Zhang H, Deng L, Sun Y, Zhang J, Deng W, Yang W. Multichannel gradient piezoelectric transducer assisted with deep learning for broadband acoustic sensing. *ACS Appl Mater Interfaces*. **2023**;*15*:12146.
41. Wang S, Luo Z, Liang J, Hu J, Jiang N, He J, Li Q. Polymer nanocomposite dielectrics: understanding the matrix/particle interface. *ACS Nano*. **2022**;*16*:13612.
42. Fu Y, He H, Zhao T, Dai Y, Han W, Ma J, Xing L, Zhang Y, Xue X. A self-powered breath analyzer based on PANI/PVDF piezogas-sensing arrays for potential diagnostics application. *Nano-Micro Lett*. **2018**;*10*:76.
43. Wang S, Luo Z, Liang J, Hu J, Jiang N, He J, Li Q. Polymer nanocomposite dielectrics: understanding the matrix/particle interface. *ACS Nano*. **2022**;*16*:1361.
44. Tian G, Deng W, Xiong D, Yang T, Zhang B, Ren X, Lan B, Zhong S, Jin L, Zhang H, Deng L, Yang W. Dielectric microcapacitance for enhancing piezoelectricity via aligning MXene sheets in composites. *Cell Rep Phys Sci*. **2022**;*3*: 100814.
45. Zhang J, Yang T, Tian G, Lan B, Deng W, Tang L, Ao Y, Sun Y, Zeng W, Ren X, Li Z, Jin L, Yang W. Spatially confined MXene/PVDF nanofiber piezoelectric electronics. *Adv Fiber Mater*. **2024**;*6*:133.
46. Li T, Wei Z, Jin F, Yuan Y, Zheng W, Qian L, Wang H, Hua L, Ma J, Zhang H, Gu H, Irwin MG, Wang T, Wang S, Wang Z, Feng Z-Q. Soft ferroelectret ultrasound receiver for targeted peripheral neuromodulation. *Nat Commun*. **2023**;*14*:8386.
47. Meng N, Ren X, Santagiuliana G, Ventura L, Zhang H, Wu J, Yan H, Reece M, Bilotti E. Ultrahigh beta-phase content poly(vinylidene fluoride) with relaxor-like ferroelectricity for high energy density capacitors. *Nat Commun*. **2019**;*10*:4535.
48. Tian G, Deng W, Gao Y, Xiong D, Yan C, He X, Yang T, Jin L, Chu X, Zhang H, Yan W, Yang W. Rich lamellar crystal baklava-structured PZT/PVDF piezoelectric sensor toward individual table tennis training. *Nano Energy*. **2019**;*59*:574.
49. Yang T, Deng W, Tian G, Deng L, Zeng W, Wu Y, Wang S, Zhang J, Lan B, Sun Y, Jin L, Yang W. Modulating piezoelectricity and mechanical strength via three-dimensional gradient structure for piezoelectric composites. *Mater Horiz*. **2023**;*10*:5045.
50. Mackie P. The classification of viruses infecting the respiratory tract. *Paediatr Respir Rev*. **2003**;*4*:84.
51. Zhang Q, Liang Q, Zhang Z, Kang Z, Liao Q, Ding Y, Ma M, Gao F, Zhao X, Zhang Y. Electromagnetic shielding hybrid nanogenerator for health monitoring and protection. *Adv Funct Mater*. **2018**;*28*:1703801.
52. Zhang H, Zhang J, Hu Z, Quan L, Shi L, Chen J, Xuan W, Zhang Z, Dong S, Luo J. Waist-wearable wireless respiration sensor based on triboelectric effect. *Nano Energy*. **2019**;*59*:75.
53. Sun J, Xiu K, Wang Z, Hu N, Zhao L, Zhu H, Kong F, Xiao J, Cheng L, Bi X. Multifunctional wearable humidity and pressure sensors based on biocompatible graphene/bacterial cellulose bioaerogel for wireless monitoring and early warning of sleep apnea syndrome. *Nano Energy*. **2023**;*108*: 108215.

54. Cheraghi Bidsorkhi H, Faramarzi N, Ali B, Ballam L, D'Aloia A, Tamburrano A, Sarto S. Wearable graphene-based smart face mask for real-time human respiration monitoring. *Mater Des*. **2023**;*230*: 111970.
55. Liu J, Wang H, Liu T, Wu Q, Ding Y, Ou R, Guo C, Liu Z, Wang Q. Multimodal hydrogel-based respiratory monitoring system for diagnosing obstructive sleep apnea syndrome. *Adv Funct Mater*. **2022**;*32*:2204686.
56. Ning C, Cheng R, Jiang Y, Sheng F, Yi J, Shen S, Zhang Y, Peng X, Dong K, Wang Z. Helical fiber strain sensors based on triboelectric nanogenerators for self-powered human respiratory monitoring. *ACS Nano*. **2022**;*16*:2811.

Publisher's Note Springer Nature remains neutral with regard to jurisdictional claims in published maps and institutional affiliations.

Springer Nature or its licensor (e.g. a society or other partner) holds exclusive rights to this article under a publishing agreement with the author(s) or other rightsholder(s); author self-archiving of the accepted manuscript version of this article is solely governed by the terms of such publishing agreement and applicable law.